Supporting Information:

Investigation of facet-dependent performance of α-Fe_2O_3 nanocrystals for heavy metals determination by atripping voltammetry

Wei-Hong Xu, Qiang-Qiang Meng, Chao Gao, Jing Wang, Qun-Xiang Li,* Jin-Huai Liu, and Xing-Jiu Huang*

EXPERIMENTAL SECTION

Chemical. All chemicals used were of analytical grade and were used as received without any further purification. All chemicals were purchased from Sinopharm Chemical Reagent Co., Ltd. (China). Acetate buffer solutions of 0.1 M with pH 5 were prepared by mixing stock solutions of 0.1 M acetic acid (HAc) and sodium acetate (NaAc). Milli-Q water (18 MΩ cm in resistivity, Millipore Corporation) was used throughout the experiment.

Apparatus. The scanning electron microscopy (SEM) images were taken by a FEI Quanta 200 FEG field emission scanning electron microscope. The TEM and HRTEM images analyses were carried out on a JEM-2010 microscope. XRD was performed on a D/MaxIIIA X-ray diffractometer (Rigaku Co., Japan), using Cu Ka (λ_{Ka}=1.5418 Å) as the radiation source. The nitrogen adsorption and desorption isotherms at 77 K were measured with a Micromeritics ASAP 2020 M analyzer. The Brunauer, Emmett, and Teller (BET) equation was used to obtain the specific surface areas. The Pb^{2+} concentrations were determined in the liquid phase using inductively coupled plasma atomic emission spectrometry (ICP-AES, Jarrell-Ash model ICAP 9000). Electrochemical experiments were recorded using a CHI 660D computer-controlled potentiostat (ChenHua Instruments Co., Shanghai, China). A conventional three-electrode system consisted of a glassy carbon working electrode (GCE, 3 mm diameter), an Ag/AgCl as the reference electrode and a platinum wire as the counter electrode.

Synthesis. The synthesis of α-Fe_2O_3 nanocubes, nanoplates, and nanorods was based on the reported methods.[1, 2] α-Fe_2O_3 nanocubes: Briefly, oleic acid (20 mL), NaOH (2 g), and ethanol (20 mL) were mixed thoroughly by stirring. Afterward, 40 mL of water with 0.004 mol Fe^{3+} precursor was added to the mixed solution. Then, the mixed reactants were transferred into a Teflon-lined stainless steel autoclave and heated in an oven at 180 ºC for 10h. The autoclave was then cooled to room temperature, and the products were collected and washed with Milli-Q water and ethanol several times, respectively, and finally dried in an oven at 60 ºC for 10h. α-Fe_2O_3 nanoplates: Briefly, $FeCl_3.6H_2O$ (1 g) was dissolved under vigorously stirring in ethanol (40 mL) with Milli-Q water (2.8 mL). Afterwards, sodium acetate (3.2 g) was added under stirring. Then, the mixture was sealed in a Teflon-lined stainless steel autoclave and heated at 180 ºC for 12h. Upon cooling to room temperature, the obtained products were washed with Milli-Q water and ethanol several times, respectively, and dried at 60 ºC for 12h. α-Fe_2O_3 nanorods: Briefly, $FeSO_4.7H_2O$ (2.78 g) and CH_3COONa (3.28 g) were dissolved in 50 mL of Milli-Q water under magnetic stirring. After stirring vigorously for a period at 40 ºC, yellow slurry was formed. The products were collected and washed with Milli-Q water severals times and dried at 60 ºC under vacuum for 4h. The porous α-Fe_2O_3 nanorods were obtained by calcining the products at 300 ºC for 2h in air.

Electrode Fabrication. The construction of the α-Fe_2O_3 nanostructures on the surface of GCE was performed as follows: 5 mg of the α-Fe_2O_3 nanostructures was suspended in 1 mL of Milli-Q water to form a suspension. The suspension was then briefly sonicated for 30s in order to disperse the nanostructures. A 4 μL aliquot of this suspension was pipetted onto the surface of a freshly polished GCE and evaporated at room temperature.

Electrochemical Experiments. Square wave anodic stripping voltammetry (SWASV) was used for Pb^{2+} detection under optimized conditions. A deposition potential of −1.1 V was applied for 120 s to the working electrode by the reduction of Pb^{2+} in 0.1 M NaAc−HAc (pH 4.0). The anodic stripping (reoxidation of metal to metal ions) of electrodeposited metal was performed in the potential range of −1.0 to 0 V with step

potential of 4 mV, amplitude of 25 mV, and frequency of 15 Hz. A desorption potential of 0 V for 150 s was performed to remove the residual metals under stirring condition. The individual detection of Zn^{2+}, Cd^{2+}, Cu^{2+}, and Hg^{2+} has been performed at the same experimental conditions. All experiments were performed at room temperature under air atmosphere.

Computational Details. The Density Function Theory (DFT) calculations were performed by using the projector augmented wave potentials as implemented in the Vienna ab-initio simulation package (VASP) code.[3, 4] We use PBE as exchange correlation potential.[5] The wave functions were expanded in plane waves with a kinetic energy cutoff of 500 eV. The periodically repeated simulation (2×2), (2×2) and (1×1) cells include slabs of 15, 11, and 12 layers to model the α-Fe_2O_3 (012), (001) and (110) surfaces, respectively, as shown Fig. S9. The vacuum between the slabs is 12 Å. The atomic positions of the top four substrate layers and Pb atom are fully relaxed whereas the atoms in these bottom substrate layers are fixed at their equilibrium bulk positions. In our calculations, a 2×2×1 Monkhorst-Pack k-point is used to sample the surface Brillouin zone. The atomic positions are optimized until the residual forces vanished within 0.02 eV/Å. The optimized lattice constants of the bulk α-Fe_2O_3 (a = b = 4.78 Å, c = 13.35 Å) and the c/a ratio is 2.79 are close to the previous theoretical reports and experimental c/a ratio values 2.73(a = b = 5.03 Å, c = 13.75 Å).[6]

The adsorption energies (E_{ads}), defined as $E_{ads} = E_{Pb/surface} - (E_{surface}+E_{Pb})$, of Pb atom on α-$Fe_2O_3$ (012), (001) and (110) surfaces were calculated. Here, E_{Pb} is the atomic energy of single isolated Pb atom, while $E_{surface}$ and $E_{Pb/surface}$ are the total energies of the surface and the Pb atom adsorbing on surface, respectively. Under this definition, the more negative value stands for the more energetically stable adsorption.

To explore the diffusion behaviors of Pb on different α-Fe_2O_3 surfaces, we calculated the energy barriers of Pb diffusing on α-Fe_2O_3 three different crystal planes using the climbing image nudged elastic band method.[7] The obtained results are shown in Fig. S10.

Randles-Sevcik equation: $i_p = (2.69\times10^5)\ n^{3/2}\ A\ C\ D^{1/2}\ v^{1/2}$, where i_p is the peak current, n is the number of electrons, A is the surface area of the working electrode (cm^2), C is the bulk concentration of the electroactive species (mol L^{-1}), D is the diffusion coefficient of the electroactive species (~6.605×10^{-6} cm^2 s^{-1} for $K_3[Fe(CN)_6]$), and v is the scan rate of voltammograms (V s^{-1}). The active surface area of the nanocrystals modified GCE are evaluated to be 0.035 cm^2 (α-Fe_2O_3 nanocubes), 0.049 cm^2 (α-Fe_2O_3 nanoplates), 0.041 cm^2 (α-Fe_2O_3 nanorods), and 0.0563 cm^2 (bare GCE) according to the Randles-Sevcik equation (Fig. S11).

3σ method: The 3σ LOD is calculated from 3SD/S, where SD is the standard deviation of the measurements and S is the slope of the calibration graph.

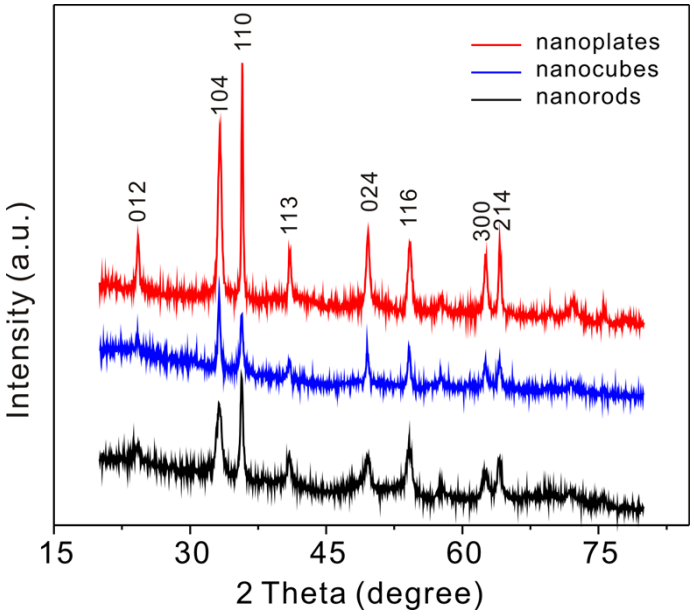

Fig. S1 XRD patterns of the three types of α-Fe_2O_3 nanostructures.

The phase formation and purity of the three types of α-Fe_2O_3 nanostructures were identified by X-ray diffraction (XRD), and are shown in Fig. S1 (Supporting Information). All XRD patterns are consistent with standard α-Fe_2O_3 with a rhombohedral hexagonal phase (JCPDS No. 33-0664). No peaks of impurities are detected, revealing the high purity of the prepared α-Fe_2O_3 nanostructures.

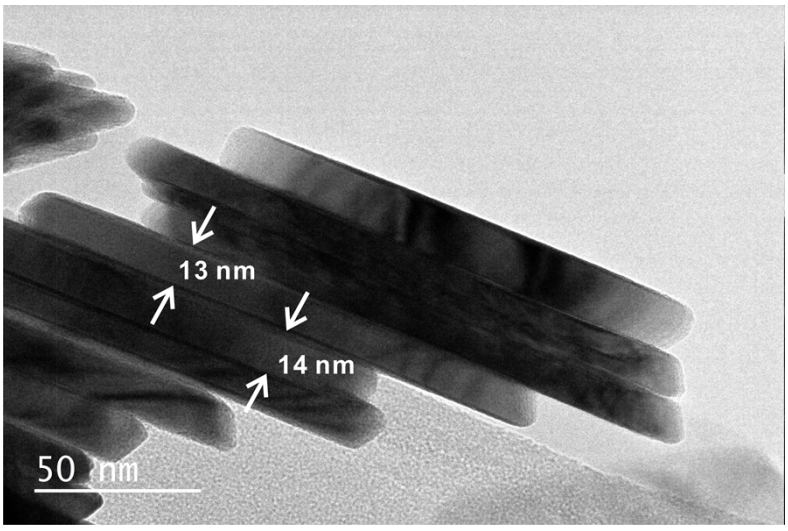

Fig. S2 A representative TEM image of α-Fe_2O_3 nanoplates. The thickness of the nanoplates is about 13-16 nm.

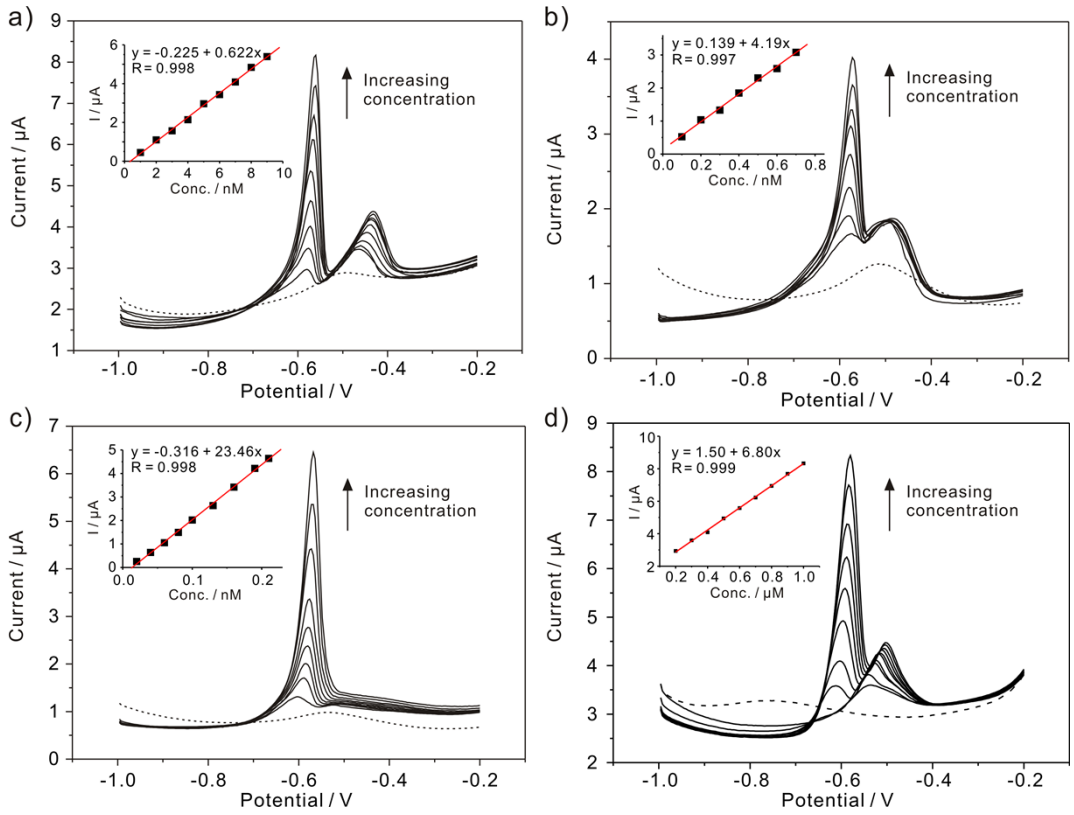

Fig. S3 Typical SWASV response of (a) α-Fe_2O_3 nanocubes, (b) α-Fe_2O_3 nanoplates, (c) α-Fe_2O_3 nanorods modified GCE, and (d) bare GCE for analysis of Pb^{2+} in different concentration ranges. Insets in panels a, b, c, and d are corresponding linear calibration plots of peak current against Pb^{2+} concentrations, respectively. Supporting electrolyte: 0.1 M NaAc-HAc solution (pH 5.0); deposition potential, -1.2 V (vs.SCE (saturated calomel electrode)); deposition time, 120 s; amplitude, 25 mV; increment potential, 4 mV; frequency, 15 Hz.

Fig. S3 shows selections of typical SWASV curves for Pb^{2+} stripping analysis in 0.1 M NaAc-HAc solution (pH 5.0) at the different α-Fe_2O_3 nanostructures modified electrodes. For α-Fe_2O_3 nanocubes modified GCE (Fig. S3a), in a concentration range of 1 to 9 nM, two stripping peaks were observed, the first peak occurred at between -0.583 and -0.559 V; and a second stripping peak appeared at potentials of -0.467 to -0.428 V. As the concentration was increased further, two peaks were found to increase. For nanoplates modified electrode, two SWASV peaks were also observed, occurring at similar potentials within a relatively low concentration range of 0.1-0.7 nM (Fig. S3b). Fig. S3c shows a selection of typical SWASV curves for Pb^{2+} in the range of 0.02-0.2 nM at nanorods modified GCE. It is strikingly clear that, within this

concentration range, only a single stripping peak was observed in the SWASV response, which was seen to shift slightly to -0.599-0.566 V with increasing concentration. We should point out that, aiming at more sensitive electroanalysis, the origin of the double stripping peak of Pb^{2+} in previous SWASV data on nanocomposites modified electrodes has been generally either ignored or tentatively attributed to some aspect of the metal deposit on the electrode surface. Recent results have shown that the two peaks are intimately related to the different metal morphologies on the polycrystalline boron doped diamond (pBDD) surface.[8]

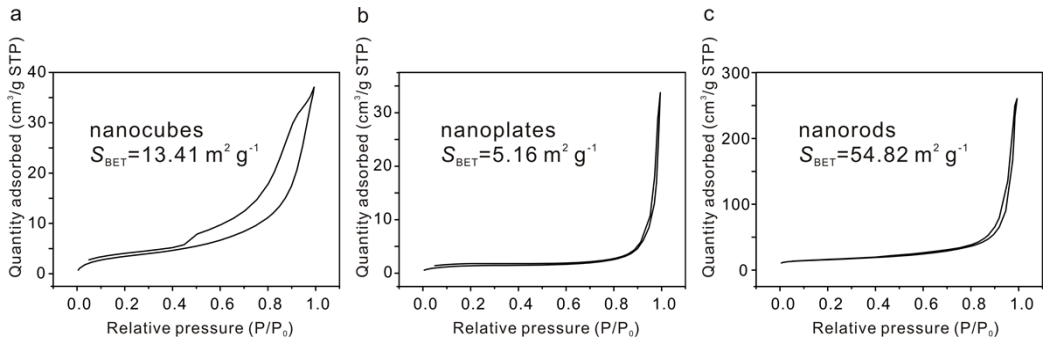

Fig. S4 N_2 adsorption-desorption isotherms of α-Fe_2O_3 nanocubes (a), nanoplates (b), and nanorods (c). The measured specific surface areas for α-Fe_2O_3 nanocubes, nanoplates, and nanorods are 13.41, 5.16, and 54.82 m^2 g^{-1}, respectively.

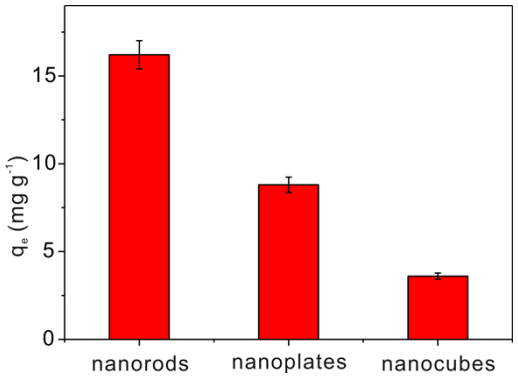

Fig. S5 Comparison of the maximum adsorption capacity for Pb^{2+} on α-Fe_2O_3 nanorods, nanoplates, and nanocubes, respectively.

The adsorption measurement was conducted in 0.1 mol L^{-1} NaAc-HAc (pH= 5.0) in order to be consistent with electrochemical conditions (see Fig. S5). Fig. S5 shows that the maximum Pb^{2+} adsorption capacity is about 3.6, 8.8, and 16.2 mg g^{-1} for α-Fe_2O_3 nanocubes, nanoplates, and nanorods, respectively, which is highly consistent with the order of the electrochemical activities for these three types of α-Fe_2O_3 nanostructures. That is because adsorption is also strongly related with the surface atomic arrangement and unsaturated dangling bonds of the exposed facets.[9] Very recently, it is found that the exfoliated ZrP shows the strongest adsorption capacity toward Pb^{2+} among other heavy metal ions, thereby resulting in selective electrochemical response consequently.[10] Highly selective adsorption of a polypyrrole/reduced grapheme oxide nanocomposite toward Hg^{2+} caused electrochemically selective detection of Hg^{2+}.[11] These studies confirmed that the adsorption performance of a non-conductive modifier is directly consistent with its electrochemical ability. Thus, on the basis of the experimental results, it can be concluded that the different exposed facets of α-Fe_2O_3 nanostructures are attributed to the different electrochemical performances primarily.

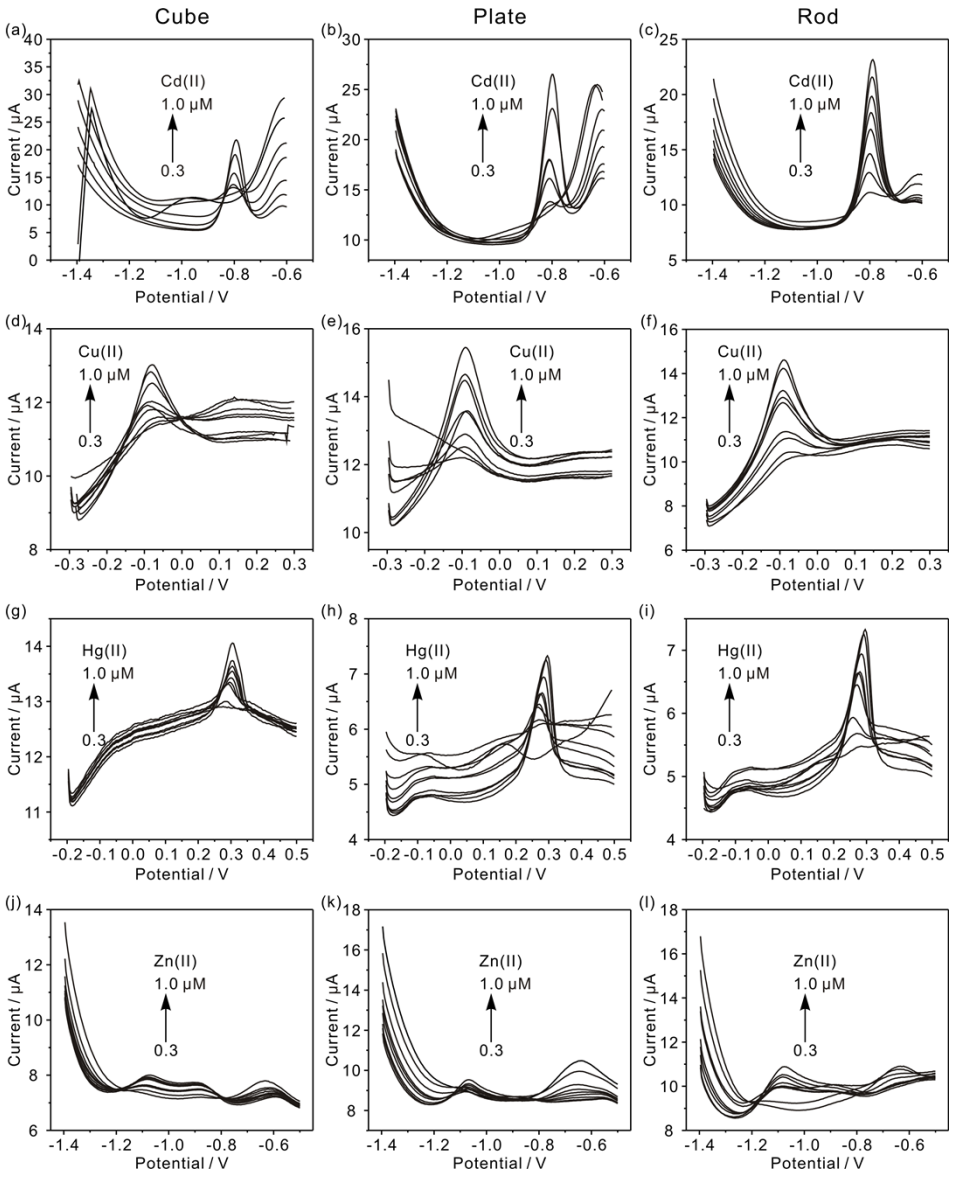

Fig. S6 Typical SWASV response of α-Fe_2O_3 nanocubes (a, d, g, and j), α-Fe_2O_3 nanoplates (b, e, h, and k), and α-Fe_2O_3 nanorods (c, f, i, and l) modified GCE for analysis of Cd^{2+} (a, b, and c), Cu^{2+} (d, e, and f), Hg^{2+} (g, h, and i) and Zn^{2+} (j, k, and l) in different concentration ranges. Supporting electrolyte: 0.1 M NaAc-HAc solution (pH 5.0); deposition potential, -1.2 V (vs.SCE (saturated calomel electrode)); deposition time, 120 s; amplitude, 25 mV; increment potential, 4 mV; frequency, 15 Hz.

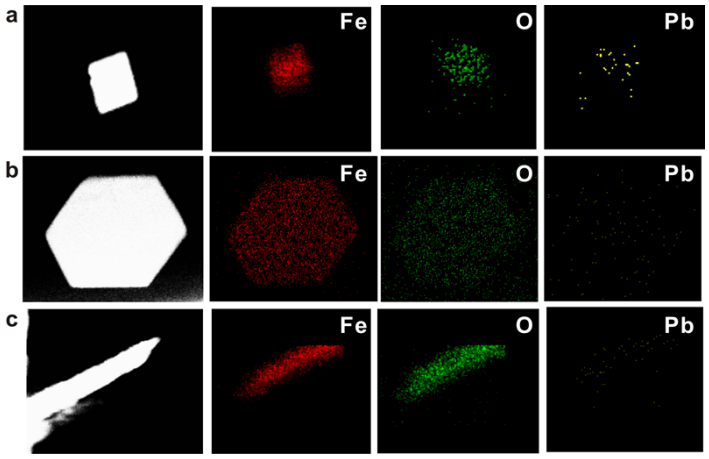

Fig. S7 STEM-EDS elemental mapping images of α-Fe_2O_3 nanocubes (a), nanoplates (b), and nanorods (c), respectively, after adsorption of Pb^{2+}.

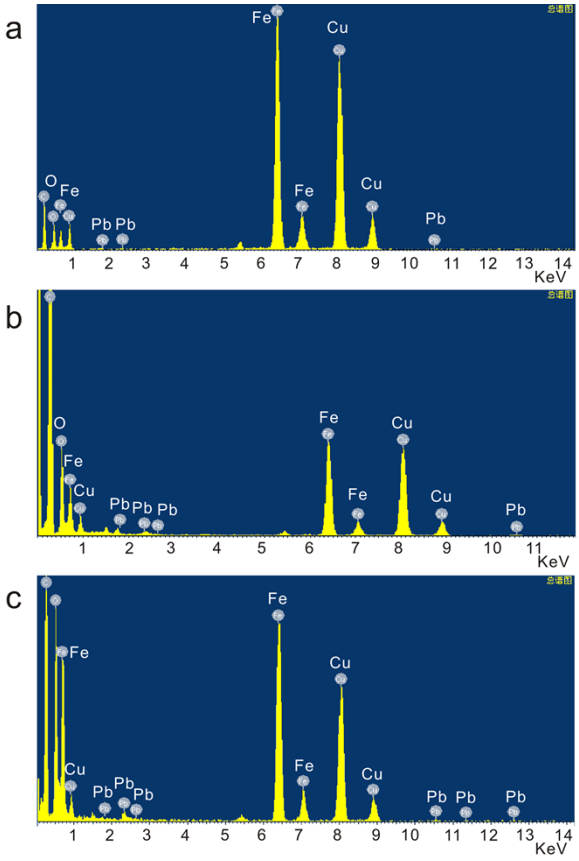

Element	Weight %	Atomic %
Fe	97.47	92.60
O	2.21	7.32
Pb	0.33	0.008

Element	Weight %	Atomic %
Fe	81.58	57.36
O	17.28	42.42
Pb	1.14	0.22

Element	Weight %	Atomic %
Fe	78.73	53.10
O	19.81	46.64
Pb	1.45	0.26

Fig. S8 EDX spectra of different facets of α-Fe_2O_3 nanostructures after adsorption of Pb^{2+} and the corresponding element content. (a) α-Fe_2O_3 nanocubes; (b) α-Fe_2O_3 nanoplates; (c) α-Fe_2O_3 nanorods.

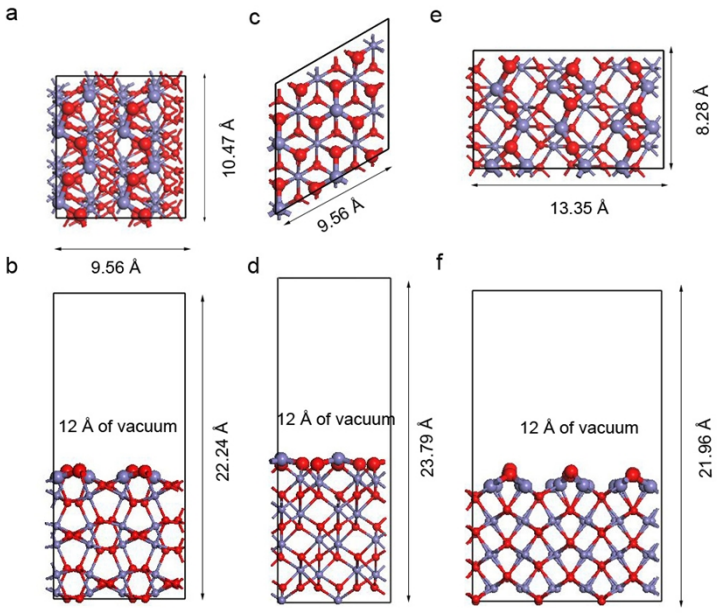

Fig. S9 The top and side views of the slab models for α-Fe_2O_3 different surfaces: a), b) (012), c), d) (001), e), f) (110). The red and light gray spheres stand for O and Fe atoms, respectively.

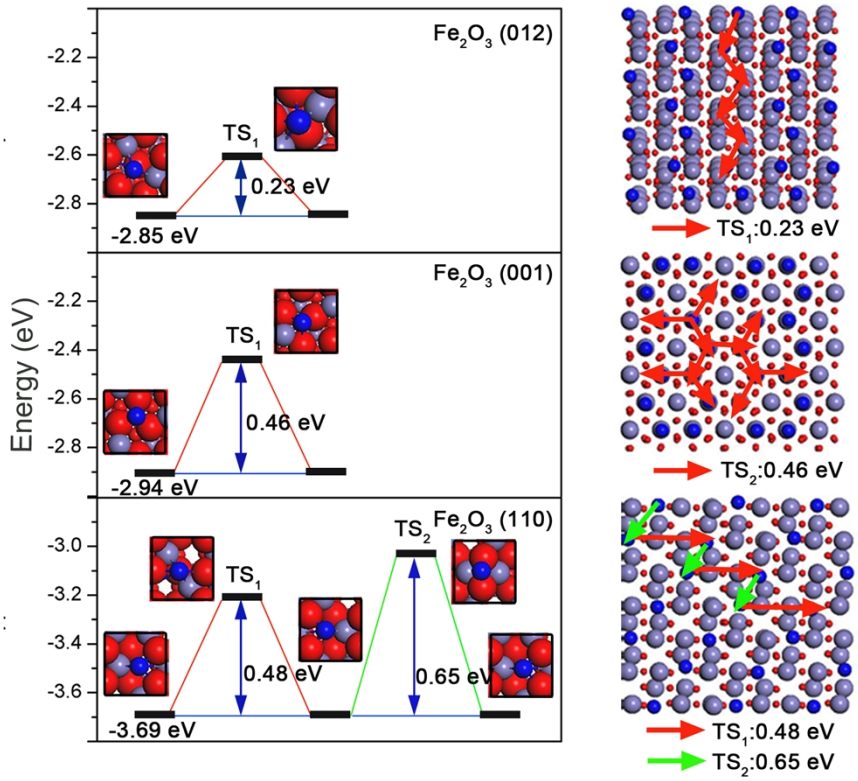

Fig. S10 Left panel: the transition-state (TS) barriers of Pb on α-Fe_2O_3 (012), (001) and (110) surfaces, top view of these optimized stable adsorption and TS structures. Right panel: the diffusion paths of Pb on α-Fe_2O_3 surfaces are labeled with solid arrow lines of different colors for clarity. Pb reaches the nearest neighboring stable adsorption site after overcoming the TS barriers.

The calculated diffusion energy barriers of Pb on α-Fe_2O_3 (012), (001) and (110) surface are predicted to be 0.23, 0.46 and 0.65 eV, respectively. We can see that the diffusing ability of Pb follows (012) > (001) > (110) as shown in the Fig. S10. However, it is important to mention that all the energy barriers are relatively low. Considering diffusion paths and energy barriers of Pb diffusing, Pb can effectively diffuse on these crystal planes under the experimental conditions. Thus, the selective adsorption of Pb on different exposed crystal facets is attributed to the selective electrochemical response, which is the determining factor in detection of HMIs for α-Fe_2O_3 nanostructures modified GCE.

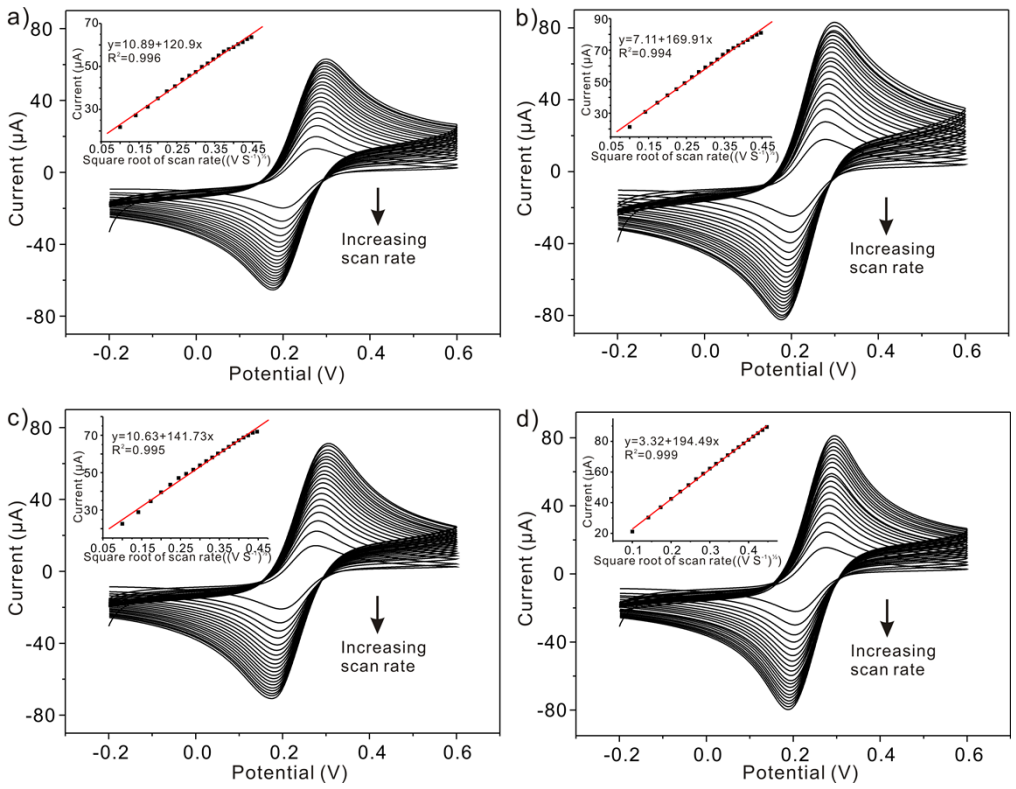

Fig. S11 Scan rate study (from 0.01 to 0.2 V s^{-1}) in the solution of 5 mmol L^{-1} $Fe(CN)_6^{3-/4-}$ containing 0.1 mol L^{-1} KCl at (a) α-Fe_2O_3 nanocubes, (b) α-Fe_2O_3 nanoplates, (c) α-Fe_2O_3 nanorods, and (d) bare modified GCE, respectively. Insets are the corresponding plots of current versus the square root of the scan rate with a linear trend line.

Table S1. Physicochemical properties of α-Fe_2O_3 nanocubes, nanoplates, and nanorods.

sample	length (nm)	width (nm)	height (nm)	specific surface area (m^2 g^{-1})	dominant facets
nanocubes	24-26	24-26	24-26	13.41	{012}
nanoplates	-	128-132	13-16	5.16	{001}
nanorods	200	10-20	10-20	54.82	{110}

Table S2. The comparison of sensitivity and limit of detection (LOD, 3σ method).

		Nanorod	Nanoplate	Nanocube
Cd^{2+}	Sensitivity (μA cm^{-2}/ nM)	0.727 (±0.029)	0.648 (±0.026)	0.444 (±0.018)
	LOD (nM)	0.038 (±0.020)	0.066 (±0.030)	0.044 (±0.025)
Hg^{2+}	Sensitivity (μA cm^{-2}/ nM)	0.078 (±0.003)	0.076 (±0.009)	0.037 (±0.002)
	LOD (nM)	0.033 (±0.010)	0.062 (±0.010)	0.11 (±0.020)
Cu^{2+}	Sensitivity (μA cm^{-2}/ nM)	0.162 (±0.007)	0.154 (±0.006)	0.106 (±0.002)
	LOD (nM)	0.028 (±0.010)	0.053 (±0.012)	0.040 (±0.010)
Zn^{2+}	Sensitivity (μA cm^{-2}/ nM)	0.050 (±0.002)	0.041 (±0.002)	0.012 (±0.001)
	LOD (nM)	0.086 (±0.020)	0.024 (±0.010)	0.12 (±0.030)

1 Y. Wang, J. L. Cao, S. R. Wang, X. Z. Guo, J. Zhang, H. J. Xia, S. M. Zhang and S. H. Wu, *J. Phys. Chem. C*, 2008, **112**, 17804-17808.
2 X. M. Zhou, J. Y. Lan, G. Liu, K. Deng, Y. L. Yang, G. J. Nie, J. G. Yu and L. J. Zhi, *Angew. Chem. In. Ed.*, 2012, **51**, 178-182.
3 G. Kresse and J. Hafner, *Phys. Rev. B*, 1993, **47**, 558-561.
4 P. E. Blochl, *Phys. Rev. B*, 1994, **50**, 17953-17979.
5 J. P. Perdew, K. Burke and M. Ernzerhof, *Phys. Rev. Lett.*, 1996, **77**, 3865-3868.
6 G. Rollmann, A. Rohrbach, P. Entel and J. Hafner, *Phys. Rev. B*, 2004, **69**, 165107.
7 G. Henkelman, B. P. Uberuaga and H. Jonsson, *J. Chem. Phys.*, 2000, **113**, 9901-9904.
8 L. A. Hutton, M. E. Newton, P. R. Unwin and J. V. Macpherson, *Anal. Chem.*, 2011, **83**, 735-745.
9 H. Wang, J. T. Yang, X. L. Li, H. Z. Zhang, J. H. Li and L. Guo, *Small*, 2012, **8**, 2802-2806.
10 L. Wang, W. H. Xu, R. Yang, T. Zhou, D. Hou, X. Zheng, J. H. Liu and X. J. Huang, *Anal. Chem.*, 2013, **85**, 3984-3990.
11 Z. Q. Zhao, X. Chen, Q. Yang, J. H. Liu and X. J. Huang, *Chem. Commun.*, 2012, **48**, 2180-2182.